Progress in Oceanography 79 (2008) 120–137

Contents lists available at ScienceDirect

Progress in Oceanography

journal homepage: www.elsevier.com/locate/pocean

Vertical structure variability in a seasonal simulation of a medium-resolution regional model of the Eastern South Pacific

Boris Dewitte [a,b,*], Marcel Ramos [c,d], Vincent Echevin [e], Oscar Pizarro [f,g], Yves duPenhoat [a]

[a] LEGOS/IRD/CNES, 14 Av. Edouard Belin, 31400 Toulouse, France
[b] IMARPE, Esquina de Gamarra y General Valle S/N, Chucuito Callao, Peru
[c] Programa de Postgrado en Oceanografía, Departamento de Oceanografía, Universidad de Concepción, Concepción, Chile
[d] Centro de Estudios Avanzados en Zonas Áridas, Facultad de Ciencias del Mar, Universidad Católica del Norte, Chile
[e] LOCEAN/IRD/IPSL, Laboratoire d'Océanographie et de Climatologie: Expérimentation et Approches Numériques, Paris, France
[f] Departamento de Geofísica, Universidad de Concepción, Concepción, Chile
[g] COPAS, Universidad de Concepción, Concepción, Chile

ARTICLE INFO

Article history:
Received 28 February 2007
Received in revised form 2 May 2008
Accepted 14 October 2008
Available online 21 October 2008

Keywords:
Extra-tropical Rossby waves
Critical latitude
Coastal-trapped wave
Peru–Chile Undercurrent

ABSTRACT

A seasonal simulation from a medium-resolution ocean general circulation mode (OGCM) is used to investigate the vertical structure variability of the Southeast Pacific (SEP). The focus is on the extra-tropical Rossby wave (ETRW) variability and associated forcing mechanism. Some aspects of the model mean state are validated from available observations, which justifies a vertical mode decomposition of the model variability. The analysis of the baroclinic mode contributions to sea level indicates that the gravest mode is dominant over most of the domain at all frequencies. Annual variability is on average twice as large as the semi-annual variability which is confined near the coast for all the modes. The first baroclinic mode contribution to the annual cycle exhibits a clear westward propagation north of the critical latitude. The higher-order modes only contribute near the coast where they are associated with vertically propagating energy. The residual variability, which is the energy at all timescales other than annual and semi-annual periods peaks offshore between ~20°S and ~30°S for all baroclinic modes. The third baroclinic mode also exhibits a relative maximum variability off the coast of Peru south of the critical latitude of the annual cycle (~13°S), where the Peru–Chile Undercurrent is the most intense. Sensitivity experiments to the atmospheric and boundary forcing suggest that the residual variability results from the non-linear interaction between annual Rossby waves and the mean flow, while the annual ETRWs in the model result from the summed-contribution from both the local wind stress and remote equatorial forcing. Overall the study extends the classical analysis of sea level variability in the SEP based on linear theory, and suggests that the peculiarities of the baroclinic modes need to be taken into account for interpreting the sea level variability and understanding its connection with the equatorial variability.

1. Introduction

The coastal ocean off Peru and Chile is characterized by permanent upwelling cells in the north due to prevailing trade winds, and by seasonal upwelling in the south. This region also contains the Peru–Chile Current System (PCCS), extending from central Chile (~40°S) to northern Peru (~4°S) (cf. Strub et al., 1998). The PCCS is complex, composed of several surface and subsurface currents, and subject to large seasonal and interannual variabilities. The PCCS has been of interest to the oceanographic and climatic community because climate variability off Peru and Chile is strongly connected to tropical Pacific variability, with the South American coast behaving as an extension of the equatorial wave guide over a wide range of frequencies (Shaffer et al., 1997; Pizarro et al., 2001, 2002; Vega et al., 2003). The PCCS is also intensely productive in terms of fish catch, even when compared to other Eastern Boundary Current (EBC) regions (Strub et al., 1998; Carr, 2002). Thus, the socio-economical impact of climatic events such as ENSO (El Niño Southern Oscillation) has been large over the region. The offshore regional variability (for example as evidenced by the TOPEX/POSEIDON data; Stammer, 1997) also exhibits a strong spatial heterogeneity, reflecting a complex combination of forcing mechanisms of the extra-tropical Rossby waves (ETRW) in a region where mixing processes can significantly impact water mass properties (Yeager and Large, 2004). An important question remains how the extra-tropical Rossby waves 'ventilate' the PCCS.

Altimetric data indicates that ETRWs contribute to sea level variability over a wide range of frequencies (Chelton and Schlax,

* Corresponding author. Address: LEGOS/IRD/CNES, 14 Av. Edouard Belin, 31400 Toulouse, France.
E-mail address: bxd@imarpe.gob.pe (B. Dewitte).

0079-6611/$ - see front matter © 2008 Published by Elsevier Ltd.
doi:10.1016/j.pocean.2008.10.014

1996), but also that dispersion from linear theory is likely important (Killworth et al., 1997). As an illustration, Fig. 1 presents the maximum amplitude and phase of the sea level seasonal cycle from altimetric data over 1992–2004. Fig. 1 reveals several interesting features: the phase lines tend to be parallel to the coast north of ~30°S, illustrating the large scale structure and offshore propagation of the signal. The pattern of maximum amplitude for sea level reflects the change in the annual ETRW with latitude with the largest values north of a line from ~30°S at the coast to ~15°S at 90°W, and minimum values south of this line. Further to the south and to the west, the analysis captures prominent mesoscale eddy activity (Chaigneau and Pizarro, 2005). The overall pattern does however not show clear westward propagation suggesting that non-linear processes are at work or that it results from a complex combination of baroclinic modes with different propagation speeds. These observations motivate this study, which attempts to document the ETRW and associated processes at seasonal timescales in the SEP.

ETRW models connected to coastal-trapped wave models have been used to explore sea level and thermocline anomalies near the Chilean coast on a variety of timescales (Vega et al., 2003; Ramos et al., 2006). However, in reduced gravity models of the ocean's response to wind forcing (Qiu et al., 1997), many physical processes are ignored including (1) the coupling of Rossby waves to bottom topography (Killworth and Blundell, 1999), (2) vertical mixing, (3) projection of momentum on the different vertical modes and the coupling among them, and (4) the effects of vertical shear (Killworth et al., 1997; deSzoeke and Chelton, 1999; ColindeVerdiere and Tailleux, 2006) or (5) bottom roughness (Tailleux and McWilliams, 2001). More sophisticated numerical models include these effects but become difficult to interpret.

Here a vertical modal decomposition of a general circulation model is used to explore the seasonal variability in SEP and understand the mechanisms that control the oceanic response to wind and remote forcing. Of particular interest is how the dynamical modes are forced in the model and the connection to equatorial variability via coastal-trapped waves and the radiation of the ETRW north of the critical latitude (Clarke and Shi, 1991). Stated another way, we explore whether the SEP can be considered linear on the different timescales that encompass the seasonal cycle. In addition, the study provides a description of the baroclinic mode variability in the region, as a complement to studies based on linear models (Vega et al., 2003; Ramos et al., 2006). In particular, linear models typically use a single mode with a dissipation term (Rayleigh type) to account for energy lost from the surface to the deep ocean. Such an approach assumes that dissipation occurs through vertical propagation of the Rossby wave (McCreary, 1984; Kessler and McCreary, 1993), a process that, to the author's knowledge has not been investigated for the extra-tropical latitudes in a realistic framework. The modal decomposition used here should provide insights on such process, and extend classical analyses based on the linear theory.

The work is structured as follows. The model, data and method are briefly described in Section 2. In Section 3, mean circulation and the propagating variability are analysed. In Section 4, the vertical mode decomposition is presented and the propagating characteristics of the baroclinic modes are investigated. Section 5 focuses on local and boundary forcing through sensitivity experiments with modified forcing conditions. These experiments permit assessing the degree of 'linearity' of the ESP system as a function of timescale. Section 6 summarizes and discusses relevance of the model findings to our understanding of the ESP dynamics.

2. Model, data and method

2.1. Model

The primitive equation OPA model at 1/3° resolution (fully described by Madec et al., 1998) has been set up for the ESP, in the area between 5°S and 40°S, 92°W and 70°W. This model has 31 z-levels in the vertical with 10 m intervals between 0 and 100 m, and 500 m at 4750 m depth. The model has a rigid lid and the sea surface height is calculated diagnostically. The horizontal diffusion on the tracers and velocity is bilaplacian with a constant coefficient of 1.4×10^{11} m^4/s. The model resolution is sufficient to allow some eddies to be resolved explicitly, but the intensity of the resolved mesoscale activity remains low compared to observations.

Open boundary conditions are specified for velocity (barotropic stream function and baroclinic velocities), and for the tracers tem-

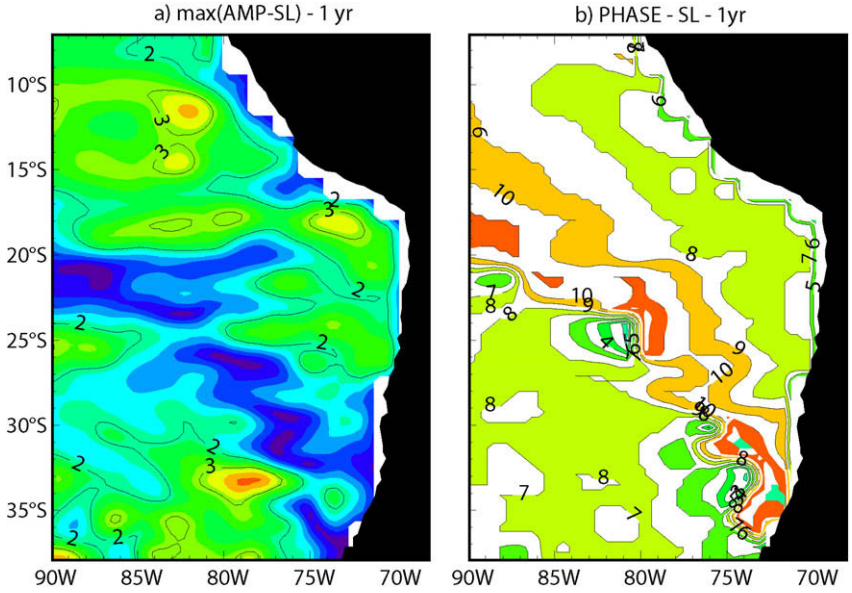

Fig. 1. Maps of the (a) amplitude and (b) phase (annual harmonic) of the seal level as derived from TOPEX/POSEIDON satellite data. Units is cm for the amplitude and calendar month for the phase ('1' corresponds to 'January'). The annual harmonic was smoothed with a three-grid-point-width boxcar average.

perature and salinity for inflow into the model domain. Tracers are advected out of the domain with an upstream advection scheme. A sponge layer is also included to damp propagating waves. The sponge layer is narrow on the north open boundary (1.7°) and wider for the south and west open boundaries (5.3°).

The model is forced at the boundaries with a climatology of the temperature, salinity and velocity fields obtained from an ORCA $2° \times 2°$ global interannual simulation. The global model was forced by ERS winds over 1992–2000 (cf. Lengaigne et al. (2002) for details). The surface forcing of the regional model consists of monthly climatological ERS winds (Bentamy et al., 1996), NCEP heat fluxes (Kalney et al., 1996) and CMAP precipitation fluxes (Xie and Arkin, 1996) over 1992–2000.

Three manipulative experiments used the settings in Table 1, which correspond to different local (heat and momentum fluxes) and open-ocean boundary forcings. The control run simulation, called CR, used a seasonally varying forcing both at the open boundaries (OBs) and at the air–sea interface, whereas the other two simulations explore the impacts of seasonality at the open boundaries (experiment called OBmean) and the momentum fluxes at the air-sea interface (experiment called TXTYmean) by cancelling one or the other. These manipulations OBmean and TXYmean are analysed in Section 5.

Simulations were run for 7 years with climatological forcing. The first 3 years are considered as the spin up period and only the last 4 years are analyzed.

2.2. Data

2.2.1. Gridded satellite winds ERS

Wind products are from CERSAT (http://www.ifremer.fr/cersat) (Bentamy et al., 1996). ERS 1–2 scatterometer measurements have a 50 km spatial resolution and a 500 km-wide swath. These satellites covered the global ocean in 3 days and operated from January 1991 to December 2000. A monthly climatology was computed for 1992–2000 and was used to force the model.

2.2.2. Mixed layer depth (MLD)

Global MLD climatology is from de Boyer Montégut et al. (2004). It was estimated using *in situ* temperature profiles, for which the MLDs are estimated using a difference criterion of 0.2 °C between the surface reference depth (10 m) and the base of the mixed layer. A gridded monthly product is then built on a $2° \times 2°$ spatial grid.

2.2.3. T/P + ERS altimetric data

Sea Level Anomaly (SLA) maps were supplied by AVISO (CLS, Toulouse, France) from 1993 to 2004. The maps result from an optimal interpolation of combined altimetric data from TOPEX/POSEIDON and ERS1/2 missions (Le Traon et al., 1998) on a $1/4° \times 1/4°$ grid every week. The SLAs are built by removing from the measurements the mean sea surface over 7 years (1993–1999). The precision of this product is of about 2–3 cm rms.

2.2.4. Levitus data set

The World Ocean Database 2001 (Conkright et al., 2002) or so-called Levitus data set (Levitus et al., 1998) for temperature was used to derive the mean thermocline depth and to check the model seasonal density structure.

2.2.5. Sea surface temperature (SST)

Two products were used to estimate the mean SST over the model domain: (1) the so-called Reynolds data set (Reynolds and Smith, 1994) on a $1° \times 1°$ resolution grid, with data over 1990–2002; and (2) the 9 km resolution SST from Advanced Very High Resolution Radiometer (AVHRR; Vazquez et al., 1995) from PODAAC (http://podaac-www.jpl.nasa.gov/products/product102.html) over 1990–2002.

2.3. Method

To understand the dynamic response of the model ocean to variable atmospheric forcing, we used a vertical modal decomposition of ocean density structure. Dynamic vertical modes form a complete orthogonal set that can describe any perturbations of density. We follow Dewitte et al. (1999) who analyzed the interannual variability of equatorial currents and sea level. We have made two simplifying assumptions here. First, we assume that linearization is appropriate. Linearization requires that interface deviations be small relative to mean layer thicknesses, which is probably true on seasonal time scales. Second, we assume that the Wentzel–Kramers–Brillouin (WKB) approximation is appropriate, allowing the analysis to be done independently at each location. This approximation requires that the background state changes over a length scale that is large relative to the wavelength of the perturbations. Although the mean stratification can experience drastic changes over short distances in the region of interest (in particular near the coast where isotherms rise), the method is justified *a posteriori* by the model results, which provide a meaningful dynamical interpretation of the ocean's response to variable atmospheric forcing (see also Thompson et al. (2002) for the North Pacific). The density change length scale off the coast is also much larger than the local Rossby radii (see Fig. 8 of Section 4.1). The WKB approximation in the context of topographic variations is justified by Killworth and Blundell (1999), who argue that while coastal topographic slopes do impact local baroclinic modes and their phase speeds, on a basin-wide average, topographic variations do not influence the overall propagation characteristics of the long-wavelength Rossby waves.

As noted by Wunsch (1997) in his modal decomposition of mooring observations in the World Ocean, modal decomposition has the advantage over, say, Empirical Orthogonal Functions (EOFs) in that it keeps dynamically distinct features separate. EOFs mix the different vertical modes, and only work well when the mode energy levels are very different.

In order to confirm/infirm the propagating nature of the derived baroclinic mode contributions, we used Extended-EOF decomposition (Weare and Nasstrom, 1982). This method often produces pairs of modes with similar spatial structure and explained variance but with a quadrature phase shift. The similar characteristics imply that these paired modes essentially describe the same propagating phenomenon. Modes which are not paired often correspond to non propagating phenomena.

Table 1
Model experiments' description.

Name	Boundary forcing	Wind stress forcing	Heat flux forcing
CR (control run)	Monthly climatology	Monthly varying climatology	Monthly varying climatology
TXYmean	Monthly climatology	Annual mean constant	Monthly varying climatology
OBmean	Mean	Monthly varying climatology	Monthly varying climatology

3. Mean circulation and propagating variability

In this section, we examine the realism of the simulation with regards to the main fields and properties that can influence the wave characteristics. In particular we focus on (1) the mean vertical stratification that determines the vertical mode structure, (2) the characteristics of the Peru–Chile Undercurrent (PCU) that is a major feature of the coastal current circulation in the ESP, and (3) the mixed layer depth that influences how the momentum flux is transmitted to the dynamics and the off-shore and coastal sea level variability.

3.1. Mean state

3.1.1. SST

The mean SST of the CR model is presented in Fig. 2a, where it can be compared to both the Reynolds and AVHRR observations (Fig. 2b and c). The model simulates the main pattern of SST, with a realistic representation of the basin-wide meridional gradients and position of the isotherms. Near the coast, the Peru upwelling (delimited by the 20 °C isotherms) is captured and compares fairly well to the Reynolds estimate. At finer spatial scale, comparison of the two products permits evaluation of the model's ability to simulate the permanent upwelling cells along the Peru–Chile coast. Due to the relatively low resolution of the model (1/3°), the simulated cross-shore SST gradients (not present in the Reynolds SST) are weaker north of ~20°S (Fig. 2a) compared to the observed AVHRR SST (Fig. 2c), which results in substantially cooler SST in the model. On the other hand, off the coasts of central and southern Chile, temperatures are slightly warmer off-shore and cooler on shore, which indicates that the model either overestimates upwelling or that heat fluxes are not realistic or are incorrectly distributed over the mixed layer (too deep at the coast, see Fig. 5). Despites these model flaws, and although the model produces wigglings of the isotherms that are not always present in the high-resolution observations, it provides a generally realistic distribution of SST at

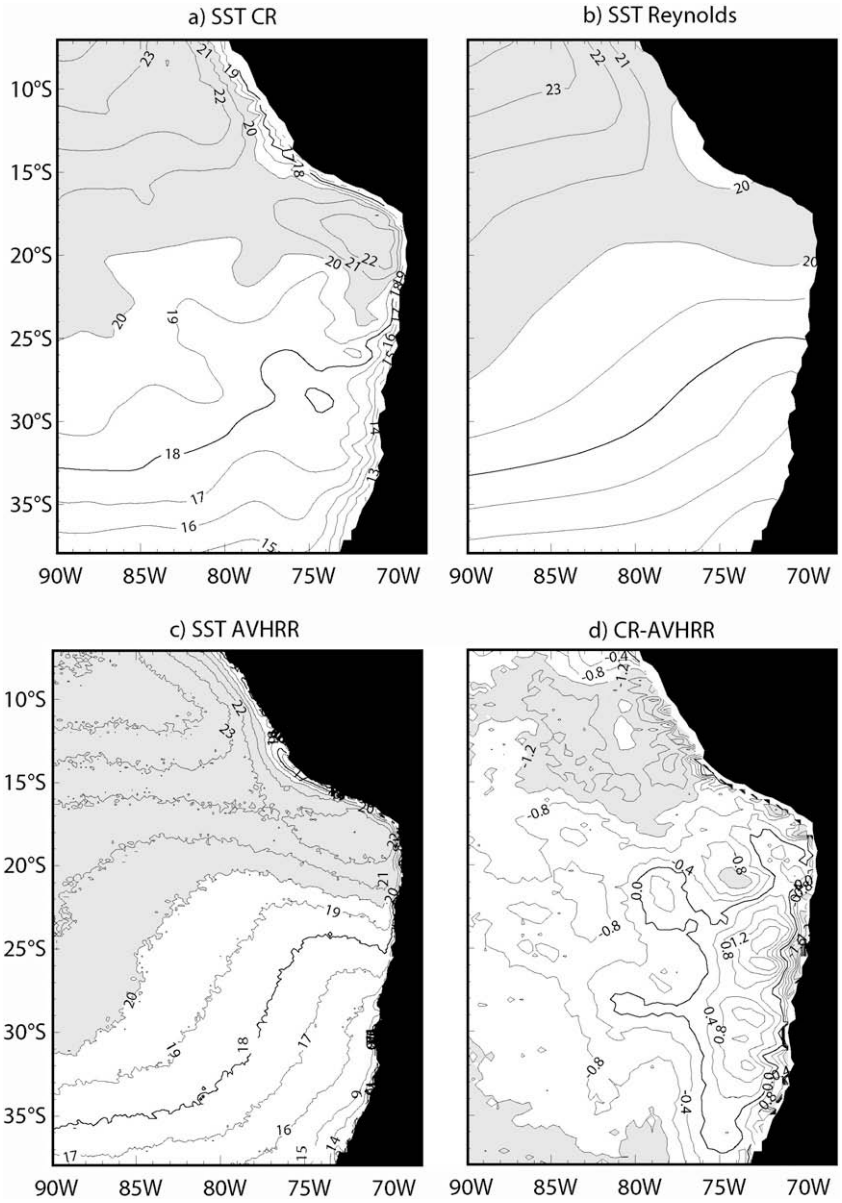

Fig. 2. SST for (a) CR, (b) the Reynolds observations (1° resolution) and (c) the AVHRR observations (9 km resolution). (d) Mean SST difference between CR and AVHRR. Unit is °C. Shading is for temperature above 20 °C and the 18 °C-isotherm is in thick line for (a)–(c). Shading is for temperature anomaly lower than −1.2 °C in (d).

a resolution that cannot be achieved from observations for the subsurface in this region of the world. This also motivates the present study.

3.1.2. Thermocline depth

The thermocline depth in the control run (CR) and in the WOA01 observations was calculated following Pizarro and Montecinos (2004) based on the depth of the maximum temperature gradient (Fig. 3). The comparison is presented in Fig. 3 which highlights the difference in resolution of the two products. The maximum depth is found at 17°S, 89°W in the model, whereas it is at 23°S; 83°W in the observations which may reflect the scarcity of the observed data in this region. Near the coast, the model thermocline does not shoal nearly as much as the observations, which is partly due to the difference in vertical resolution of the two products (higher for the model). Near 500 km offshore the model thermocline tends to be deeper than the observations. However, the mean zonal gradients in thermocline depth, when averaged between 15°S and 35°S, are similar (~0.1 m/km).

3.1.3. Peru–Chile Undercurrent (PCU)

The PCU is a well-defined, poleward, subsurface flow, which extends over the continental shelf and slope off the west coast of South America with a core located between 100 and 300 m depth. The PCU transports warm, salty equatorial subsurface water from the eastern tropical Pacific to at least as far south as 48°S (Silva and Neshyba, 1979). This water mass in turn is the main source for the coastal upwelling off Peru and northern Chile (e.g. Huyer et al., 1987) and is associated with the oxygen minimum (Wyrtki, 1963). A mean poleward flow in the PCU of 5–10 cm s^{-1} has been observed between 5°S and 12°S off Peru (Huyer et al., 1991). At 30°S off Chile, a southward mean flow of about 13 cm s^{-1} (for the period January 1993–February 1999) was observed at 230 m depth, near the PCU core over the upper slope (Pizarro et al., 2002). Like other poleward undercurrents of EBC systems, the PCU may be a return current driven by upwelling-favorable, alongshore winds blowing in the opposite direction (McCreary, 1981). Roden (1962) also showed the relevance of wind-driven Sverdrup dynamics to explain the presence of the rather strong southward transport along the coast of Peru, though he was limited by the poor quality of wind datasets available.

However, seasonal and interannual changes in the PCU off Chile and Peru are not clearly related to these winds (Huyer et al., 1991; Pizarro et al., 2001), and important seasonal variability originates on the equator (Pizarro et al, 2002). It is thus interesting to explore the mean characteristics of the PCU in the model, which will help validate the model and provide insight into PCU dynamics. Fig. 4 displays the mean characteristics (maximum along-shore velocity and depth) of the modelled PCU at 10°S and as a function of latitude. Fig. 4a can be compared to Fig. 11 of Huyer et al. (1991) although the latter is based on data of a peculiar period and corresponds to geostrophic currents only, unlike the climatological model. Despite this limitation, the 1991 figure indicates that the modelled PCU has a realistic pattern at 10°S with a minimum velocity core ~200 km off-shore and a secondary core attached to the continental slope. Its magnitude is weaker than in the observations and decreases southward, while its depth increases southward (Fig. 4b). Considering the relatively low resolution of model with regards to the cross-shore scale of this current (~50 km), the realism of the simulated PCU is encouraging with regards to the connection between equatorial and inner basin variability. In the following, to examine PCU variability, we will consider variability at the core of the mean PCU.

3.1.4. Mixed layer depth

Investigating the mean mixed layer depth in the model may provide insights on the realism of the vertical gradients in the surface layers which impacts the dynamical response of the ocean to momentum and heat flux forcing. Note that the spatial heterogeneity of the model mixed layer will be taken into account to diagnose the theoretical baroclinic mode energy distribution (see Section 4.1). Following de Boyer Montégut et al. (2004), the model mean mixed layer depth was calculated based on the temperature profile with criteria of 0.2 °C (i.e. the depth where temperature equals SST – 0.2 °C). The results are displayed in Fig. 5. The model correctly simulates the offshore deepening of the mixed layer. Further offshore, the model exhibits fine scale structures which may not be resolved by the observations. In particular, near 90°W, 20°S the model simulates a deeper mixed layer than in the observations, whereas near 78°W, 22°S it is shallower.

Summarizing, it appears the model mean state has a reasonably realistic structure that may account for PCU dynamics. It allow further investigation of its variability and associated forcing mecha-

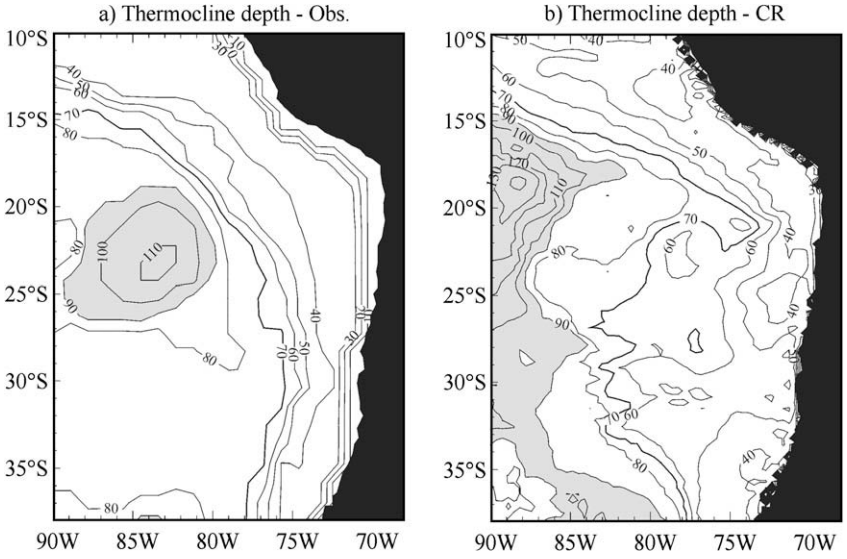

Fig. 3. Mean thermocline depth for (a) Levitus data and (b) CR. Unit is m. Shading is for depth larger than 90 m.

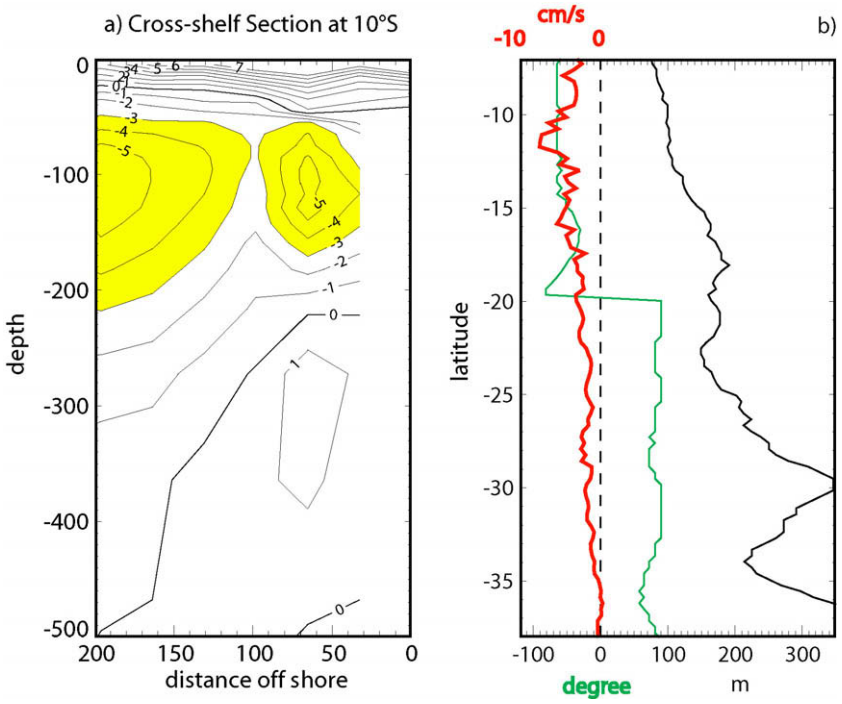

Fig. 4. Mean characteristics of the PCU in CR (negative value for southward current): (a) the cross-shelf section of current at 10°S. This figure can be compared to Fig. 11 of Huyer et al. (1991) who made an estimate of the geostrophic flow from four CTD sections at 10°S [see also Fig. 3 of Strub et al. (1998)]. Yellow shading is for values of current lower than -3 cm s^{-1}. (b) Depth of the core of the PCU (black line) and minimum mean along-shore velocity in the core of the PCU (red line) as a function of latitude (upper scale). The angle of slope of the coastline used to estimate the along-shore velocity is also plotted in green line (lower scale).

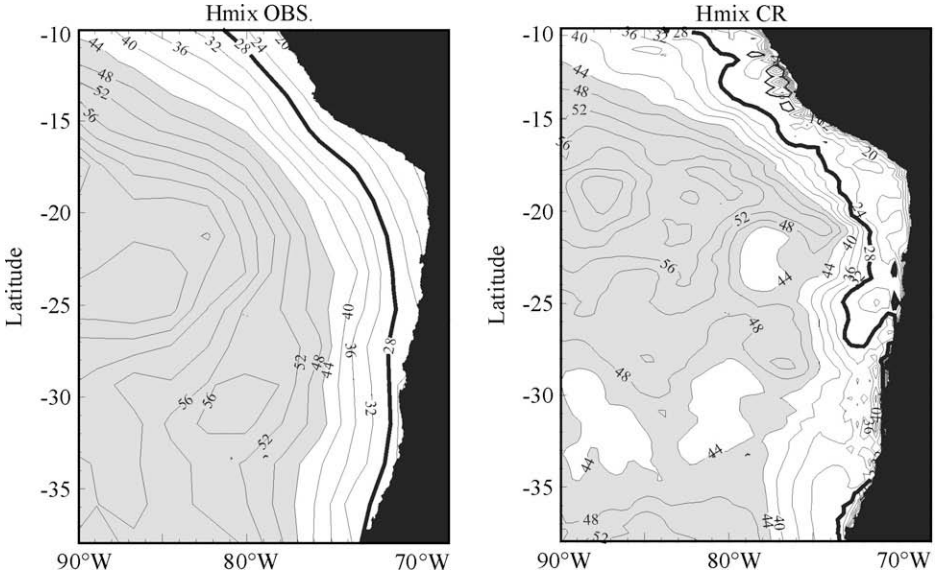

Fig. 5. Mixed layer depth for the observations (left) and the model (right). Unit is *m*. The criteria used is on temperature (dT = 0.2 °C). Shading is for depth larger than 44 m.

nisms. In the following, some aspects of the model variability are analysed.

3.2. Variability

3.2.1. Sea level

Fig. 6 displays the results of the EOF analysis of (1) the satellite-derived sea level anomalies and (2) CR. The satellite data were high-pass filtered (cut-off frequency = 1.5-year) in order to dampen interannual variability. Note however that this filtering does not completely remove the low-frequency variability contribution because the satellite seasonal cycle contains a component associated to the rectification of the interannual variability on the mean state and seasonal cycle, which is not the case for CR. This limits the comparison between the simulations and the observations.

The spatial patterns of the dominant EOF are similar for the observations and simulation over a succession of positive and negative anomalies that extend offshore more in the north than in the south. Discrepancies between the observations and the simulation are the largest south of 25°S where the variability associated with

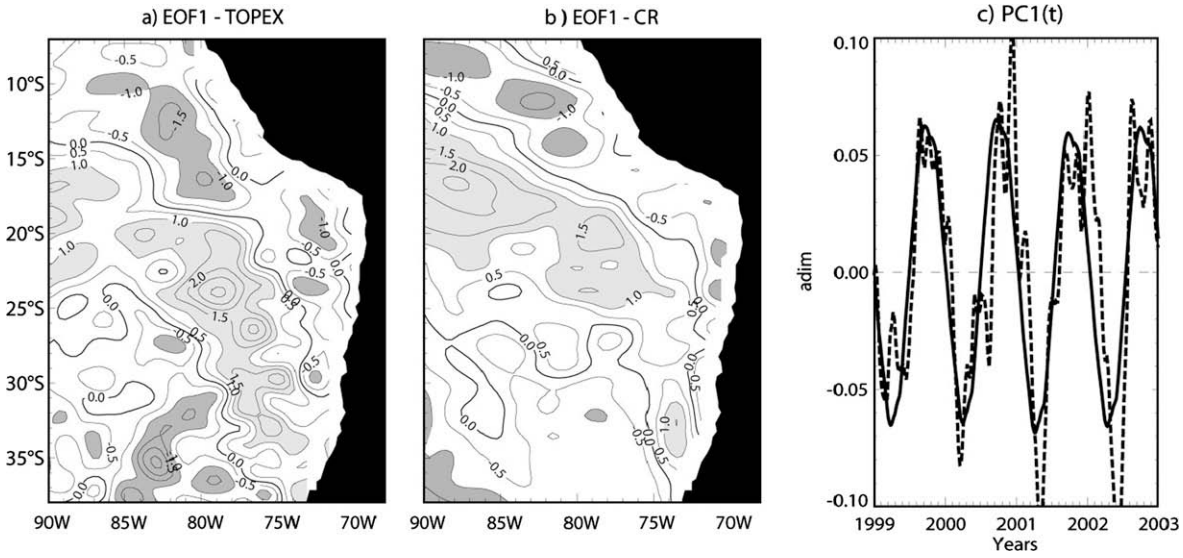

Fig. 6. Maps of the first EOF of sea level for (a) the observations as derived from TOPEX/POSEIDON data and (b) for CR. Units is cm. The associated temporal functions (in non-dimensional units) are shown in the panel (c) in plain line for CR and dashed line for the observations. Darker (lighter) shading is for value lower (larger) than −1 (1) cm. The spatial patterns were smoothed with a seven-grid-point-width boxcar average.

mesoscale eddies is significant in the observations (Chaigneau and Pizarro, 2005). This is partly due to the relatively low resolution of the model which underestimates mesoscale activity by a factor of 3 in terms of eddy kinetic energy as compared to altimetric data (not shown). It may also be related to the fact that monthly mean climatological fields forced the model so that intraseasonal variability in the model is underestimated.

The magnitude of the anomalies is on average slightly higher for the observations than for the simulation. The percentage of explained variance is 20% versus 30% for CR and the altimetric data, respectively. However, because CR uses a repetitive climatological forcing, the EOF analysis is somewhat equivalent to an Extended-EOF (E-EOF) analysis, and, as such, captures the propagating dominant mode of the variability that comes out as a pair of modes. Thus, the pattern of the second dominant mode of the EOF analysis is similar to that of the first, except that the associated temporal functions are shifted by a quarter of a period as in E-EOF analysis (not shown). This implies that the actual percentage of explained variance associated to the seasonal cycle for CR is 30% + 29% = 59%, which is much larger than for the observations. The remaining variance is associated with both the high- and low-frequency variability, which will be discussed in Section 5.

Despite these discrepancies in the spatial pattern, the associated time series of the EOFs are in phase ($c = 0.92$) (Fig. 6c). Other techniques were applied on the sea level time series, which includes E-EOF and Complex-EOF (Horel, 1984), and these lead to comparable results. For instance, the dominant CEOF mode for the model and the observations explained 86% and 53% of the variance, respectively, and exhibit comparable patterns of amplitude and phase (spatial correlation between model and observation reaches 0.50 and 0.45 for the amplitude and phase excluding the region south of a line from (20°S; 90°W) to (38°S; 73°W)).

3.2.2. PCU

As mentioned above, the PCU is a characteristic feature of the SEP. Its existence illustrates the complex vertical structure of the coastal ocean and highlights the peculiar dynamics associated with the connection to equatorial variability through coastal-trapped Kelvin waves. In the following, some aspects of PCU variability are documented through the model, which will later serve as a basis for examination of the connection between the equatorial and the inner basin variability.

The seasonal variability of the PCU has not been well documented due to scarcity of data. Pizarro et al. (2002) however documented PCU variability from a 7-year long current record over the slope and near the core of the PCU at 30°S and showed that this flow is strongly modulated at seasonal and interannual periods by Rossby waves which are in turn forced by equatorial Kelvin waves arriving at the South American coast. Ramos et al. (2006) also noted a connection at semi-annual periods between the coastal and offshore thermocline variability in northern Chile. At these timescales, the PCU, embedded in the coastal 'wave guide', exhibits a variability that is documented from the model.

Fig. 7a displays the annual and semi-annual harmonics of the PCU and wind stress along the coast as a function of latitude, with semi-annual harmonics represented over two cycles. It indicates that, whereas the semi-annual cycle of the PCU exhibits a clear southward propagation pattern, the annual cycle exhibits more latitudinal variability, reflecting a more complex forcing mechanism at annual timescale. The amplitudes of the annual and semi-annual cycles are comparable (see plain lines in Fig. 7b) with zones of relative maximum variability for the annual (semi-annual) cycle between 9°S and 13°S (9°S and 11°S) and between 27°S and 37°S (15°S and 19°S). These increases in variability along the coast take place near the critical latitudes of the semi-annual and annual periods for the first and second baroclinic modes as estimated by Clarke and Shi (1991): ∼15°S and ∼9°S for the semi-annual period and ∼37°S and ∼23°S for the annual period (see Fig. 7c). Note that the coastline shape and vertical grid configuration of the model (taking into account the changes in the continental shelf width) may explain the deviation from the Clarke and Shi (1991)'s estimate. The latter is based on 300 km segments chosen so that they approximated the deep-sea boundary (source of the topographic data is not mentioned in Clarke and Shi (1991)).

The annual harmonics of the along-shore wind may contribute to the change in propagating characteristics of the PCU variability. As noted in earlier works (Shaffer et al., 1999), the winds off the coast of Peru tend to be phase lagged (lag = ∼4–6 months) with the ones of southern Chile with a minimum variability between 17°S and 22°S (Fig. 7b). Moreover, the increase in PUC annual variability south of 25°S seems to be consistent with an increase in

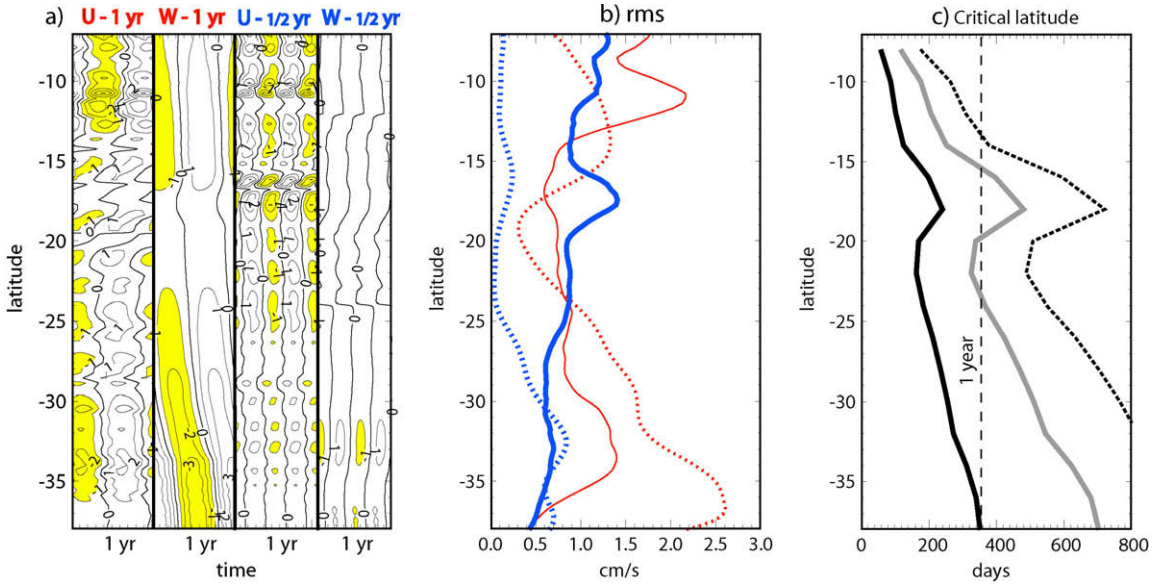

Fig. 7. PUC seasonal cycle: (a) time-latitude sections of the annual and semi-annual components of the PUC and along-shore wind stress. Negative values correspond to southward (northward) current (wind stress). Units are cm s^{-1} for currents and 10^{-2} N m^{-2} for wind stress. Each field are represented over 1-year period. Yellow shading is for values lower than −1. Unit. (b) Variability (RMS) as a function of latitude of the annual (red lines) and semi-annual (blue lines) components of the PUC (plain lines) and wind stress (dotted lines). RMS curves were smoothed with a seven-grid-point-width boxcar average. (c) Critical latitude as a function of the period for the first (black line), second (grey line) and third (dotted line) baroclinic mode as derived from Clarke and Shi (1991).

wind stress, with a lag of several months (Fig. 7a). The semi-annual component of the along-shore wind is much weaker than the annual component, which favours the free poleward propagation of the semi-annual component of the PCU.

With these few aspects of the model variability and mean state in mind, we next investigate the vertical density structure variability and associated dynamical response.

4. Vertical mode decomposition of the model variability

A vertical mode decomposition is sought in order to interpret the dynamical response of the ocean to the heat and momentum forcing and to document the off-shore propagating variability in the model.

4.1. Projection coefficient and forcing

The theoretical projection of the momentum and heat fluxes on a given baroclinic mode can be derived from the vertical mode decomposition of the mean stratification, taking into account both the heterogeneity in mixed layer depth and thermocline depth. For momentum flux, in non-dimensionalized form, the projection coefficient is written as follows, $P_n(x,y) = \frac{\frac{H}{h_{mix}}\int_{-h_{mix}}^{0}\Psi_n(x,y,z)dz}{\int_{-H_{bot}}^{0}\Psi_n^2(x,y,z)dz}$, where H is the mean thermocline depth (cf. Fig. 3b), h_{mix} the mean mixed layer (cf. Fig. 5b), Ψ_n, the vertical mode structures and H_{bot} the depth of the ocean floor. P_n is displayed in Fig. 8 for the first three baroclinic modes. The results indicate that at basin scale, a significant part of the wind stress variability projects on the first and second baroclinic modes. Due to the rising isotherms along the coast, the third baroclinic mode (and high-order modes, not shown here) contributes significantly near the coast especially north of 20°S. However, the pattern of P_n has to be interpreted in the light of the distribution of the local wind stress curl since $P_n \times \vec{\nabla}\Lambda\vec{\tau}$ is the actual forcing term of the linearized momentum equation for each mode. At the annual period, the spatial pattern of the annual harmonic of the wind stress curl forcing (Fig. 8, bottom left panel) reveals that high-order modes are not favoured near the coast between 15°S and 27°S. The region of maximum values for P_2 corresponds also to a region of minimum amplitude of the forcing. On the other hand, the regions of large P_1 are associated with the large amplitude of the annual cycle of the wind forcing, especially in the off-shore region.

Note that for heat flux, the projection coefficient has a dependency in $\frac{1}{c_n^3}$ (where c_n is the long wave phase speed for mode n) as compared to P_n (cf. Dewitte (1998)), so that for the high-order vertical modes, heat flux forcing may contribute significantly to the dynamical field variability. However, because of the weak values for phase speed, the dynamical response of the ocean has to remain mostly local and does not radiate from the forcing region.

4.2. Baroclinic mode contribution to sea level

The variability maps for the baroclinic mode contributions to sea level anomalies for the annual and semi-annual cycles and residual are presented in Figs. 9 and 10, which show that the annual cycle projects predominantly on the first baroclinic mode, whereas the semi-annual cycle is less energetic for all the modes in the inner basin. Consistent with critical latitude theory, most of the variability of the annual cycle is confined in the form of coastal-trapped Kelvin waves along the coast south of ~32°S and ~20°S for the first and second baroclinic mode contributions, respectively (see Fig. 7c for an estimation of the critical latitude as a function of baroclinic modes and frequency). The semi-annual cycle has also a maximum in variability offshore, north of ~23°S for the first baroclinic mode, again consistent with the expected theoretical critical latitude. Interestingly, the residual variability projects on all the modes and is as large as the annual variability of the first baroclinic mode. It is by far the largest contribution to the second baroclinic mode. This residual variability extends as far offshore as the annual cycle variability of the first baroclinic mode and exhibits a different spatial pattern for each of the first three modes. In particular, it exhibits a peak in the inner basin at 27°S for the first mode and at 23°S for the second mode, whereas

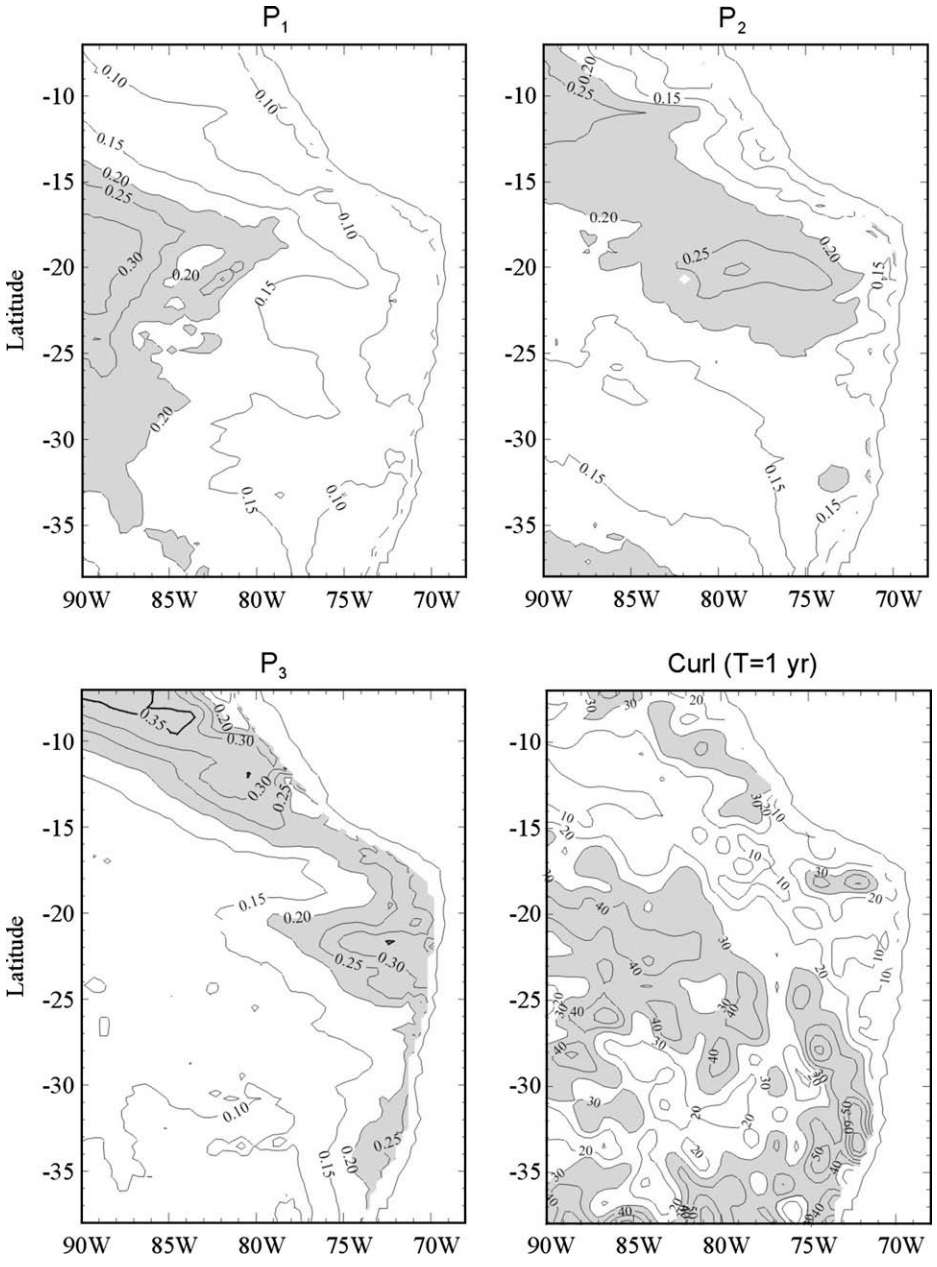

Fig. 8. Non-dimensionalized wind projection coefficient for the first three baroclinic modes and the maximum amplitude of the annual cycle of wind stress curl in 10^{-8} N m^{-3}.

for the third mode, it is the largest near (23°S–80°W) and off the coast of Peru south of ~13°S. Notably, this latter latitude corresponds to the critical latitude of the annual cycle for the third baroclinic mode (cf. Fig 7c), whereas one find the largest amplitude of the PUC along the coast of Southern Peru (Fig. 4b), suggesting wave-mean flow interaction as a source of the residual variability in this region. The summed-contribution of modes 4–18 mostly peaks within ~100 miles of the coast and south of 22°S, which is consistent with theory which predicts energy at these frequencies should remain near the coast as trapped coastal waves. Note the zone of minimum residual variability in a kind of 'shadow zone' off northern Chile for the first and second baroclinic modes and the sharp decrease in variability of the first baroclinic mode south of ~33°S (the critical latitude of the annual cycle of the first baroclinic mode). These complexities reflect the internal variability of the model, which will be further investigated in Section 5.

The first baroclinic mode is dominant over the whole basin for both the annual cycle and the residual variability. The variability of the semi-annual cycle of the first baroclinic mode is about half that of the annual cycle. In the following, we investigate the propagating characteristics of the first baroclinic mode contribution to sea level at the annual period.

4.3. Propagating characteristics

4.3.1. The first baroclinic mode extra-tropical Rossby wave

To investigate the propagating characteristics of the first baroclinic mode contribution to the annual cycle, maximum amplitude and associated phase are estimated at each grid point (Fig. 11a and b). The results indicate clear off-shore propagation of the sea level with the phase lines parallel to each other over most of the basin. Note, however, the spatial heterogeneity of the amplitude of the

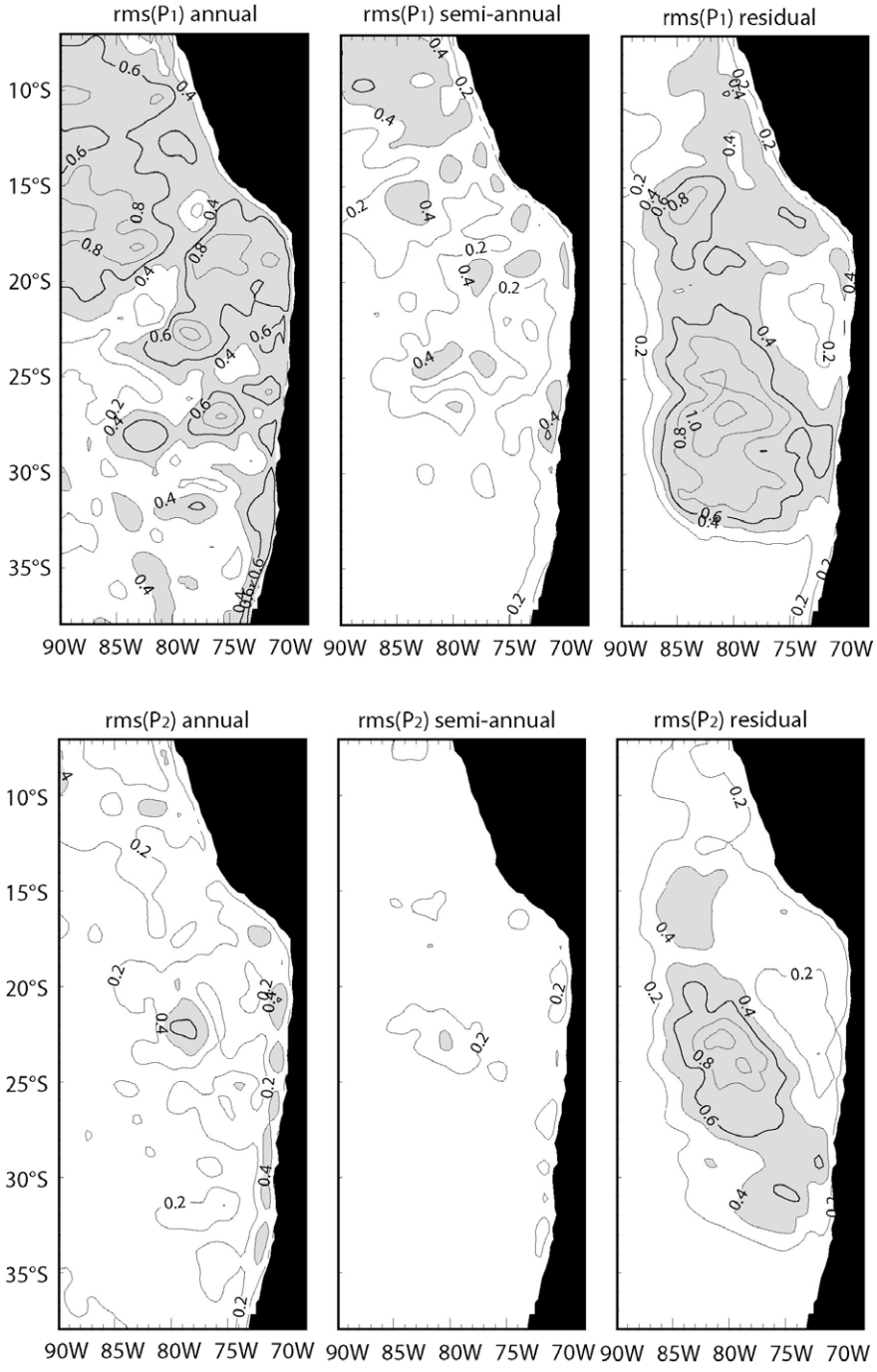

Fig. 9. Baroclinic mode energy distribution: variability (RMS) maps of first (top) and second (bottom) baroclinic contribution to sea level anomaly for the annual and semi-annual frequencies and for the residual. Units are cm. Contour intervals are every 0.2 cm. Shading is for value larger than 0.4 cm. The maps were smoothed with a three-grid-point-width boxcar average.

annual signal which traduces local wind forcing and the likely interaction between modes as suggested by the patterns of wind projection coefficients (Fig. 8). As an indication of the longitudinal extent of the propagation, we computed the distance from the coast reached after 6 months by a theoretical ETRW with phase speed $c(y) = \frac{\beta \cdot c_1^2(y)}{f^2(y)}$ (c_1 is the first baroclinic mode phase speed obtained from the vertical mode decomposition and averaged over a 5° zonal segment starting 1° from the coast). The derived curve mimics the theoretical change of phase speed with latitude (cf. white line in Fig. 11). Interestingly, the curve matches the location of the transition zone between maximum and minimum amplitude of the sea level and the region where phase lines become more erratic (Fig. 11a and b). In order to confirm the propagating nature of the signal, an E-EOF analysis was performed on the recomposed annual harmonic of the first baroclinic mode contribution to sea level. The spatial pattern of the dominant mode (which comes up as a pair) is consistent with off-shore propagation from the coast. A quantitative estimate of the wavelength from Fig. 11c (whether from the phase lines map, taking the distance between phases lines separated by 6 months, or from the E-EOF map, taking the distance of the zero line from the coast) matches the estimate from the dispersion relation of the ERWs ($\omega = -\frac{\beta k c_n^2}{f_0^2}$, see Appendix A), taking

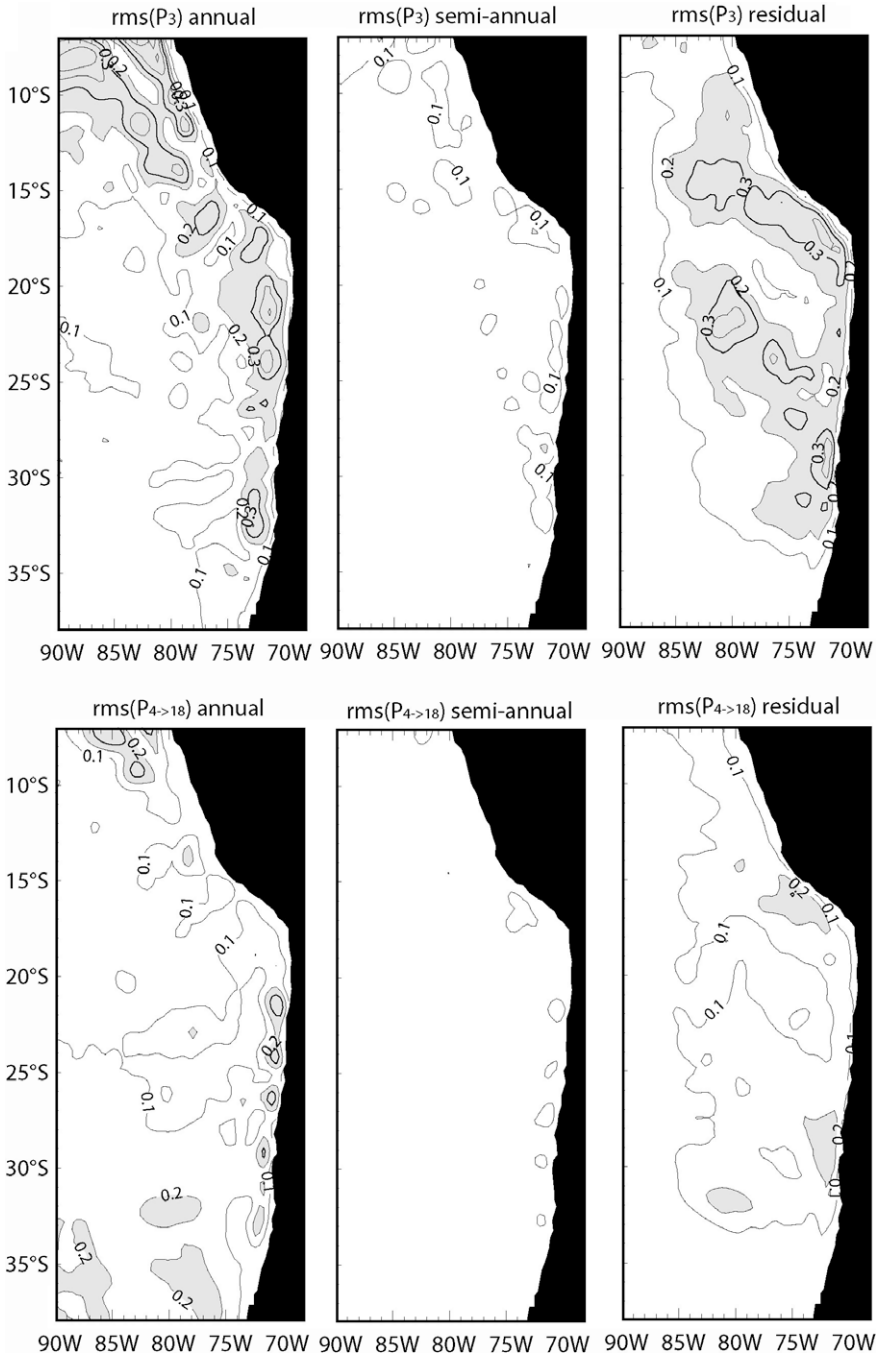

Fig. 10. Same as Fig. 9 but for the third baroclinic modes and the summed-up contributions of modes 4–18. Units are cm. Contour intervals are 0.1 cm. Shading is for value larger than 0.2 cm.

the values for c_1 as derived from the vertical mode decomposition (not shown). These comparisons confirm the off-shore propagation of first baroclinic mode ERW at annual period.

For the second baroclinic mode, off-shore propagation also occurs but is confined near the coast where the amplitude of the annual harmonic is the largest (not shown). For the third baroclinic mode, surface propagation is hardly detectable in the amplitude and phase (not shown) because of the slow phase speed and the coastal restriction of the associated variability.

As a consistency check of the model variability in terms of propagating Rossby wave, we verify in the following that the energy distribution on the baroclinic modes (as described above) is coherent with vertical propagation. Since high-order modes have a strong signature near the coast at the annual period, it is expected that they combine to form 'beams' that transfer energy downwards (McCreary, 1984). Formation of such beams would explain why the first baroclinic mode ETRW dominates the sea level variability in the model.

4.3.2. Vertically propagating energy flux

Following Dewitte and Reverdin (2000), WKB ray path theory is used to interpret wave features identified in the energy flux associated with vertical isotherm displacements. The theoretical background of the WKB ray path theory and the validity of assumptions are extended to extra-tropical latitudes and are presented in Appendix A. Ray paths correspond to the path of the energy flux

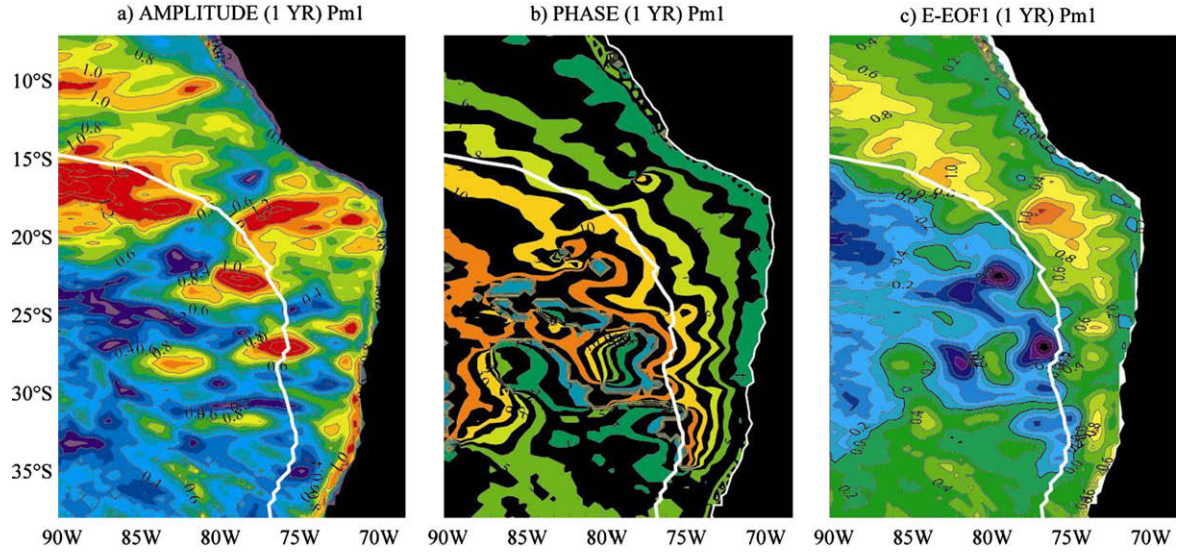

Fig. 11. Maps of the annual harmonic of the first baroclinic mode contributions to sea level anomalies (a) amplitude (in cm) and (b) phase (label '1' corresponds to January). (c) Map of the dominant E-EOF of the recomposed annual harmonic. The thick white line indicates the distance from the coast reached in 6-month by a first baroclinic mode ERW propagating with theoretical phase speed of $c = \frac{\beta c_1^2}{f^2}$.

$(u \cdot p, v \cdot p, w \cdot p)$ where (u,v,w) is the velocity vector and p is the pressure field (Eliassen and Palm, 1960). Vertical velocity w is estimated as $d\zeta/dt$, where ζ is the vertical displacement of the isotherms $\left(\zeta = \frac{T}{\frac{\partial \bar{T}}{\partial z}}\right)$. The vertical energy flux, $w \cdot p$, should be averaged over long time scales relative to the variability. If there is only one ray path and linear theory applies, the phase of the signal in vertical displacement should be constant along the ray path and the energy flux should be parallel to it. In practice however, the variability is multi-frequency, the signals originating from various areas can interfere, and the simulation is non-linear, so that the ray path concept should only be viewed as a diagnostic tool. The isotherm vertical displacements (ζ) are derived from the simulated temperature field (T) interpolated vertically on a 5 m grid using 1D cubic splines. The vertical convergence of the mean vertical energy flux associated with this field $\left\langle \frac{\partial \zeta'}{\partial t} \cdot p' \right\rangle$ quantifies the anomalous kinetic and potential energy released to the fluid through the (1) dissipation and diffusion terms (not estimated) or (2) advected from surface near the coast (or transferred by non linearities to other frequencies). Brackets denote the time average, and primes denote the annual harmonics of the individual variables.

Fig. 12 displays the annual harmonics for sections at 11°S, 17°S and 27°S. Positive values correspond to downward energy flux and extend westward and downward from the coast in the upper layers. For all sections, maximum amplitude is found near a theoretical WKB trajectory associated to a phase speed between those of the first and second baroclinic modes. The relative maximum for the 11°S section at 2000 m may be due to wave interference within the subthermocline and upward flux originating from the reflection the waves at the ocean bottom. The slope of the energy 'beam' increases with latitude, consistent with theory (cf. Appendix A). The difference between the different sections with respect to the share of energy actually reaching the deep ocean reflects the latitudinal heterogeneity of the high-order mode contribution to variability near the coast (Fig. 10) and the change in critical latitude as a function of mode order.

These results indicate that the weak surface variability of the high-order modes in the offshore region can be explained by the vertical propagation of energy by the ETRW.

5. Role of local wind stress forcing versus boundary forcing

The results presented above may be sensitive to boundary forcing. Of particular interest for the SEP is how local wind contributes to the ETRW variability, as compared to the remote equatorial forcing. Two sensitivity experiments were therefore run with the regional model, with and without seasonal change in boundary and wind forcing. The heat flux was allowed to vary as usual to simplify interpretation. Because heat flux forcing projects preferentially on the higher-order modes, it should not impact results of the manipulations presented here. The configuration of the simulations is summarized in Table 1. The TXYmean stands for the simulation using a mean wind stress forcing, whereas OBmean uses a constant open boundary condition. In order to assure that the baroclinic mode energy distribution in TXYmean and OBmean is not drastically modified by changes in the mean density structure compared to CR, which would limit the comparison between the three simulations, we verified that the mean SST, thermocline depth and mixed layer depth were similar in all the runs. The maps of the difference in mean SST between the simulations and the CR indicates that the changes in boundary forcing configuration impact the mean SST only in the coastal zone and results in SST changes no larger than + or − ~1°C (not shown). The mean thermocline depth of TXYmean and OBmean is also comparable to that in CR in the region of maximum amplitude of the first baroclinic mode (also not shown). The mean structure of the PCU was similar in all the runs (slightly larger amplitude in OBmean).

5.1. Baroclinic mode energy distribution and propagating characteristics

The vertical mode decomposition of the model runs is here described and the baroclinic mode contribution to sea level anomaly is estimated for the annual, semi-annual and residual variability. The results indicate that, as for CR, the variability in TXYmean and OBmean projects preferentially on the annual harmonics of the first mode, with the residual variability of comparable magnitude (or even larger for OBmean) to CR. Also, as for CR, the high-order mode contributions are weaker by an average factor of 2 than that of the first baroclinic mode (not shown).

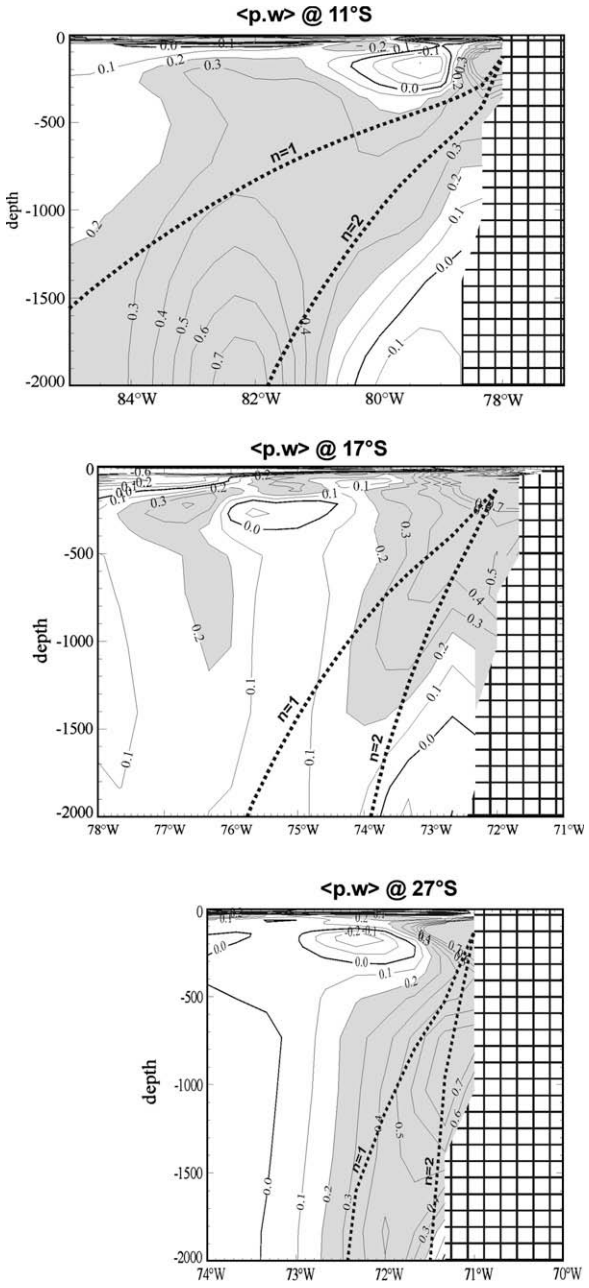

Fig. 12. Sections at 11°S, 17°S and 27°S of the vertical energy flux associated with the annual harmonic. Positive values are for downward flux. The thick dashed lines indicate the theoretical ray paths for phase speed values of the first ($n = 1$) and second ($n = 2$) baroclinic modes, respectively. Unit is 10^{-8} m^2 s^{-2}. Shading is for values larger than 2. Unit is 10^{-9} m^2 s^{-2}.

The propagating characteristic of the gravest baroclinic mode contribution to sea level at the annual period is extracted through E-EOF analysis for TXYmean and OBmean (Fig. 13). For both simulations E-EOF modes emerge as a pair with the associated time series phase-lagged by 3 months (a quarter of a period), indicating that the variability has a propagating nature. Not surprisingly the maximum variability zones of the first baroclinic mode contribution to sea level for the annual cycle are located near the coast for TXYmean (at least north of 20°S), reflecting the connection with equatorial variability. For OBmean, the variability peaks in the inner basin at various locations that are not always associated with the maximum amplitude of the annual harmonics of wind stress curl forcing (Fig. 8, bottom left panel), suggesting that the local wind stress and boundary forcing both contribute to propagation of the ETRW in CR. To illustrate these contributions, the E-EOF maps of TXYmean and OBmean are arbitrarily summed up and presented in Fig. 13c. The resulting pattern strikingly resembles the dominant E-EOF mode of CR (Fig. 11c), which suggests a quasi-linear response by the ocean at annual period. On the other hand, as will be seen in the next section, the similarity of the residual variability in all the runs indicates a non-linear response of the ocean to seasonal forcing.

5.2. Characteristics of the residual variability

The residual variability of the PCU in TYXmean and OBmean is comparable in magnitude and spatial distribution in all the runs (not shown), suggesting that the residual variability mostly results from internal dynamics and only weakly depends on the forcing. More likely, the residual variability depends on the mean alongshore current system.

To further investigate the residual variability, its low- and high-frequency components were 'separated' through filtering (a cut-off period of 1 year is used). E-EOF analysis was then performed on the filtered fields (only the first baroclinic mode contribution to sea level is considered), and the results for the dominant propagating modes plotted in Fig. 14 (only one element of the pair is displayed). For all the simulations, the high-frequency residual variability is maximal near (70°W–27°S). It also exhibits a westward-northward propagating pattern that tends to follow the mean circulation at 100 m, suggesting generation of waves through barotropic and baroclinic instability that extracts energy from the mean flow. The northward propagation may be due to the advection of the waves by the mean flow. Note that the amplitude of the signal in OBmean is more intense than in the other runs, which suggests that the wind stress may damp the instabilities near 25–27°S in CR. Along the coast of Peru, high-frequency variability is also significant for CR and TXYmean but not for OBmean suggesting that this variability mostly originates from equatorial forcing. The dominant periods of the associated time series of the E-EOF mode are ~140 days for CR and TYmean and ~250 days for OBmean.

The low-frequency component of the residual exhibits a different spatial pattern, with an 'apparent' propagating feature in the meridional direction. The variability peaks in a region centered around (80°W–30°S) for the all the runs and is larger in OBmean and TXYmean than in CR by a factor of about 2, which suggests that the non-linearities forced by the wind and boundary-forced waves in this region compensate each other and reduce the amount of energy transmitted to the longer time scales.

The characteristics of the residual sea level are suggestive of instability involving interaction between the mean circulation and the ETRWs. Cerovecki and de Szoeke (2006) studied the nature of long baroclinic wave propagation and instability in an idealized unventilated subtropical flow with vertical shear. Interestingly, their solutions from a $2^{1/2}$-layer model, both for the background flow and the perturbations, share many characteristics with the patterns of Fig. 14, which include a well-defined and narrow beam of stable waves emanating from the forcing region and propagation slightly north and westward depending on the background flow cases. These observations again support the interpretation of Fig. 14 as instability process resulting from the interaction between the annual Rossby waves and the mean circulation. Note that the residual variability is enhanced where it overlaps the region of sharp decrease in the first baroclinic mode annual ETRW amplitude, which is again consistent with the above interpretation.

6. Discussion and conclusions

A seasonal simulation from a medium-resolution OGCM is here used to investigate the variability of vertical structure in the SEP. In particular we attempt to determine if surface variability results

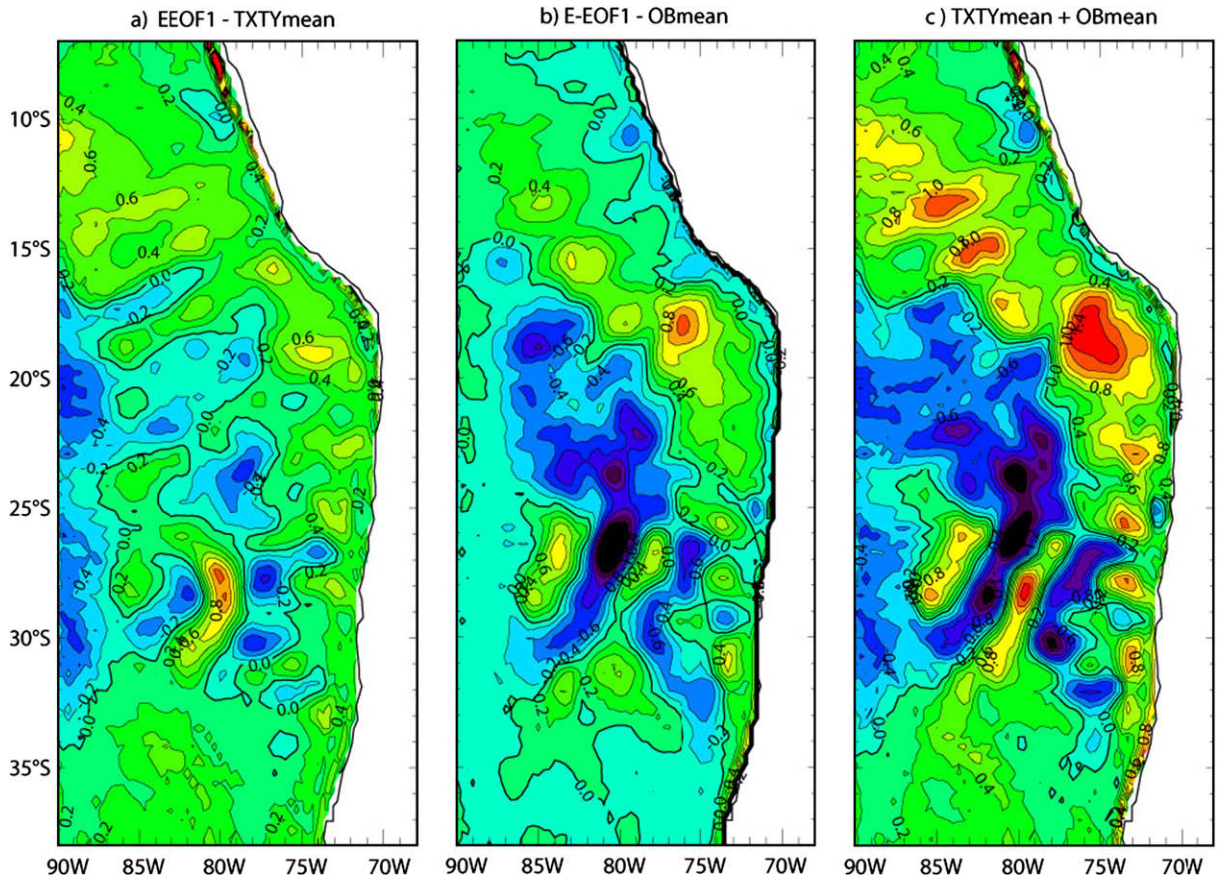

Fig. 13. Maps of the dominant E-EOF of the recomposed annual harmonic of the first baroclinic mode contribution to sea level for (a) TYmean, (b) OBmean, and (c) the sum of (a) and (b). Unit is cm.

from ETRW considering (1) the complex nature of the forcing which is both from equatorial and local origins, and (2) the presence of intraseasonal variability which, to a large extent, accounts for the non-linearity of the system. Although the model does not completely resolve coastal-trapped wave and eddy activity, it simulates much of the observed mean state and variability.

A vertical mode decomposition separated distinct modes of the variability, as evidenced by their different propagating characteristics. The decomposition works efficiently for the low baroclinic modes because the vertical structure is insensitive to the mean flow. The first baroclinic mode is the most energetic for all frequencies. The annual and residual variabilities are the most energetic for each mode (residual is total minus annual and semi-annual harmonics). The semi-annual variability is on average half that of the annual in the inner basin, whereas along the coast within the PCU, the annual and semi-annual are similar in magnitude (Fig. 7). The annual cycle of the first baroclinic mode exhibits clear westward propagation due to ETRWs forced throughout the basin and mostly in the interior. On the other hand, the second and higher-order baroclinic modes are mostly forced near the coast. Interestingly, although we make use of a full physics model, the dynamical adjustment of the ocean at annual frequency is basically linear in the sense that both the local wind stress and the boundary forcings sum to produce the sea level pattern. Another linear process associated with the annual frequency is the vertical propagation of energy that explains the large contribution of the high-order baroclinic modes near the coast, where the modes combine to form 'beams' of energy that propagate downward and westward along ray-paths that are steeper in the south, consistent with theory. Such processes have previously been documented for the equatorial annual Rossby wave (Kessler and McCreary, 1993; Dewitte and Reverdin, 2000), and are generalized here for ETRWs to verify propagation of sea level variability in the model and to interpret characteristics of the coastally trapped high-order baroclinic modes.

The results also reveal the presence of significant 'residual' variability which corresponds mostly to internal dynamics of the model physics (Fig. 14). This residual is largest near the coast and in the transition zone corresponding to the sharp decrease in amplitude and propagation of the ETRW. Interestingly, zonal change of the sea level variability in this transition zone may modulate the meridional circulation through geostrophical adjustment at a wide range of frequencies since it takes a few months ($<\sim$7–8 months) for the first baroclinic annual Rossby wave south of 10°S to cross the basin from the coast up to this zone of minimum amplitude of the annual cycle. The propagating characteristics of the residual variability are consistent with this interpretation, which suggests that the annual ETRW and the mean circulation may interact in this region (ColindeVerdiere and Tailleux, 2006; Cerovecki and de Szoeke, 2006). The possibility of such interaction certainly deserves further investigation from more specific designs of model experiments. Remarkably, results of an idealized exploration of the instability of periodic (including annual) perturbations of oceanic subtropical gyres (Cerovecki and de Szoeke, 2006) are consistent with the more realistic solution of the model.

Results of the medium-resolution model are, however, limited in a number of ways. First, it is not clear to what extent the model can reproduce coastal-trapped waves (and therefore the connection with the equatorial variability), considering that the Rossby

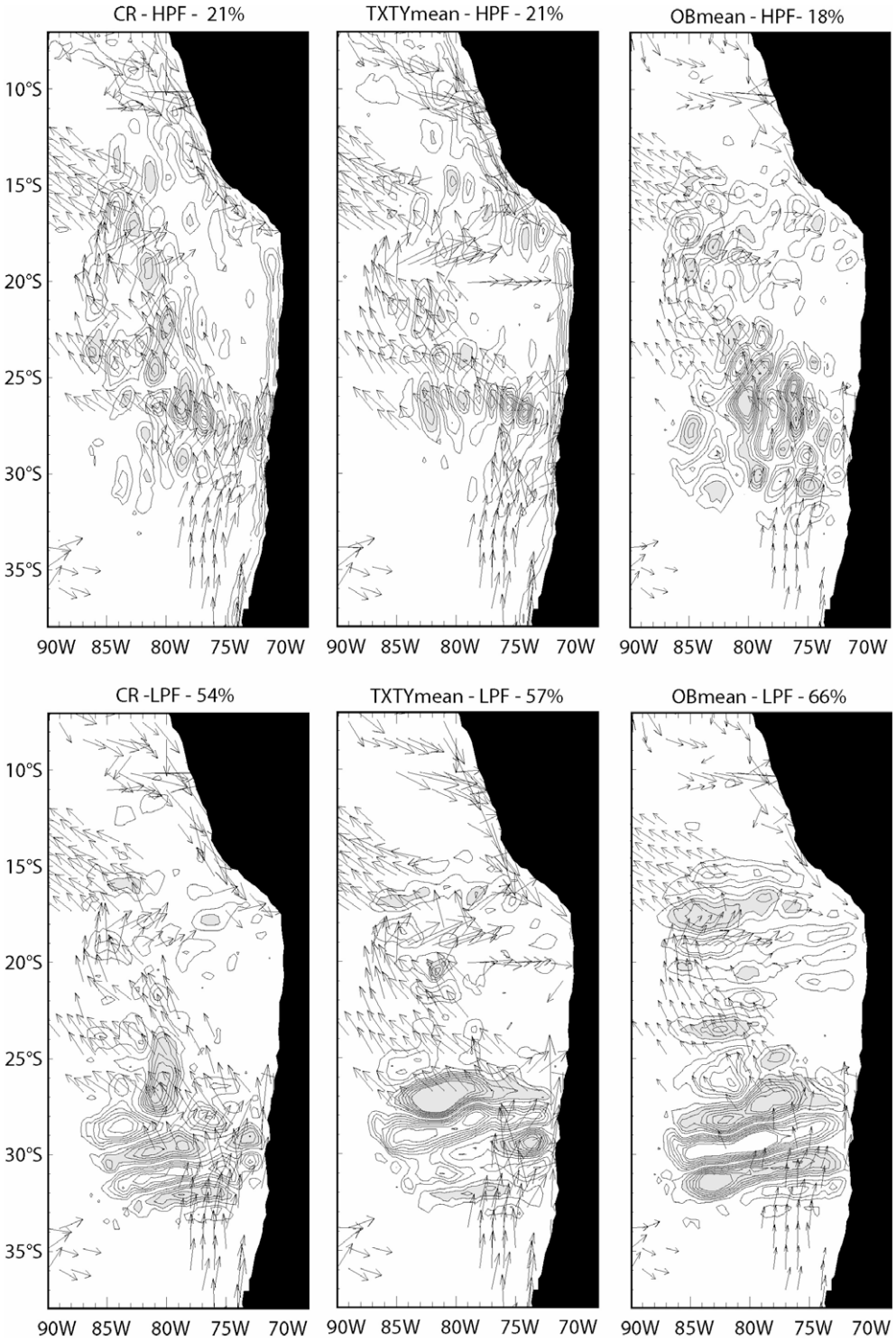

Fig. 14. Dominant E-EOF modes (one element of the pair) of the high-passed (top) and low-passed (bottom) filtered first baroclinic contribution to residual sea level for CR (left panels), TXYmean (middle panels) and OBmean (right panels). Percentage of explained variance (sum of the percentage of variance of the two elements of the pair) is indicated on top of each panel. Unit is cm. Contour interval is every 0.2 cm. Zero contours are not plotted. Shading is for values larger than 0.4 cm. The mean currents (magnitude and direction) at 100 depth are over plotted in each panel. Only the currents which either the zonal or meridional component is larger (lower) than 2 (-2) cm s^{-1} are drawn.

radius of deformation in this region is of the same order as the model resolution (the Rossby radius ranges from 150 to 30 km from ~5°S to ~40°S for the first baroclinic mode – see Chelton et al., 1998). The choice of the medium-resolution was motivated by computational cost considerations. Medium-resolution also permits meaningful interpretation of regional sea level variability. It is worth pointing out that high-resolution models are sensitive to additional parameters such as the spatial resolution of the wind forcing and the characteristics of the open-boundary conditions. For instance, in the regional high-resolution model of Penven et al. (2005), the simulated EKE has a different pattern and amplitude depending on which climatological winds – satellite Quick-

SCAT or Reanalyses product (ERA40) – are used to force the model. Variability scales of wind forcing in this region are therefore important, and the medium-resolution model is less affected by the particular wind stress product used to force the model.

Another important limitation is the seasonal forcing of the model. Considering the non-linearity of the system (as evidenced by the substantial contribution of the 'residual' variability), rectification processes at various timescales are to be expected. For instance, ENSO drastically modifies the regional mean stratification and circulation (Blanco et al., 2002) and consequently may modulate the characteristics of the annual ETRW. Such non-seasonal processes need further investigation. The model results reported here could serve as a background material for the interpretation of simulations including interannual components.

Despite these limitations, our model results show that sea level variability at the annual period consists mostly of a one-baroclinic mode response to wind and equatorial forcing. Takahashi (2005) recently found that the annual cycle of heat content in the Peru region is mainly forced by insolation, and not by the wind stress curl. He notes however that dynamical processes may produce different regional budget characteristics. The apparent conflict between our results and Takahashi's (2005) may suggest regional air–sea coupling on the annual cycle results from compensation among large dynamical signals. For instance, Kessler et al. (1998) found that annual SST in the cold tongue was consistent with solar shortwave forcing alone, but that shortwave forcing is only important because two strong forcings cancel: in their case, cooling via increased upwelling is opposed by warming associated with Tropical Instability Waves. Whether or not the heat flux in our model region is driven by horizontal or vertical advection by the ETRW will need further examination with a medium to high-resolution coupled regional model.

The model's finding of vertically propagating energy on the annual period raises the question whether such propagation might also occur at lower frequencies, including ENSO. If so, energy originating from the equatorial regions may dissipate in the subthermocline at higher latitudes. Long-term medium to high-resolution regional model simulations should provide insight on this issue.

The SEP also contains an oxygen minimum zone (OMZ; Helly and Levin, 2004) which covers a large area off-shore Ecuador, Peru and Chile and is well-marked in the subthermocline. OMZ variability and maintenance processes are poorly understood. In view of our model results, we wonder if the ETRW participates in OMZ formation and maintenance through advection of low oxygen concentration. Interestingly, the bottom of the OMZ at 300 m is located near the zone of intense residual variability in our model (not shown), which also corresponds to the westward limit of the Rossby wave annual variability. More realistic simulation of the ESP using physical–biogeomechical coupled model should help clarify this issue.

Acknowledgements

The preparation and development of this work were made possible thanks to several stays funded by ECOS (grant #C03U05) of Y. duPenhoat, B. Dewitte, O. Pizarro and M. Ramos at PROFC (Laboratorio de Procesos Oceanográficos y Clima) and LEGOS (Laboratoire d'Etude en Géophysique et Océanographie Spatiale). Dr. O. Pizarro was also supported by CNRS (Centre National de la Recherche Scientifique) while visiting LEGOS in 2001 and 2007. O. Pizarro also thanks support from Rings of Science ACT-19 project. M. Ramos was supported by a scholarship from CONICYT (Comisión Nacional de Investigación en Ciencia y Tecnología) and a thesis scholarship (AT-4040200). This study also benefited from support of the ANR (Agence Nationale de la Recherche) within the project PCCC (Peru Chile Climate Change). Computing support for running the OGCM was provided by Institut du Développement et des Ressources en Informatique Scientifique (IDRIS). The two anonymous reviewers are thanked for their constructive comments that helped improve the paper.

Appendix A. Linear formalism for vertically propagating extratropical Rossby waves

As shown by Moore and Philander (1977), the linear, inviscid equations for a β-plane ($f = f_0 + \beta y$) can be separated into vertical and horizontal components. The horizontal component yields a dispersion relation for standing wave modes in the meridional and horizontal directions

$$\omega = \frac{-\beta k}{k^2 + l^2 + f_0^2/c_n^2} \tag{A.1}$$

where l and k are the meridional and zonal wavenumbers, respectively, ω the frequency, f_0 the Coriolis parameter at some latitude (y_0) and c_n the separation constant of the vertical structure equation:

$$\frac{d}{dz}\left(\frac{d\Psi_n}{dz}\cdot N^{-2}\right) + \Psi_n c_n^{-2} = F_l \tag{A.2}$$

N is the local Brunt–Vaïsälä (or buoyancy) frequency. F_l is the projection of the forcing onto the latitudinal mode l under consideration. It is usually assumed to be zero below a certain depth close to the surface (Lighthill, 1969). Thus, the vertical structure function Ψ_n is solution of the homogeneous equation with the boundary conditions:

$$\frac{d\Psi_n}{dz} + \frac{N^2}{g}\Psi_n = 0 \quad \text{at } z = 0$$
$$\frac{d\Psi_n}{dz} = 0 \quad \text{at } z = -H \quad (H \text{ is the depth of the ocean bottom})$$

From the vertical equation a local vertical wavenumber can be defined: $m_n(x,z) = \frac{N(x,z)}{c_n(x)}$.

We now consider a motion which is the combination of the solutions of the different vertical modes for a specified l and call m the local vertical wavenumber. It is then interesting to describe the solution as if the vertical scale m^{-1} of the wave was small compared with the scale on which m varies (WKB approximation). (A.1) is then a relation between ω, m and k which can be differentiated to estimate group velocities. In this study, we consider only long zonal wavelengths. In this limit ($k^2 + l^2 \approx 0$), the dispersion relation reduces to:

$$\omega = -\frac{\beta k c_n^2}{f_0^2} \tag{A.3}$$

Given the wave frequency and phase speed, the trajectory that defines wave energy propagation can be obtained by integrating two ordinary differential equation: $\frac{dx}{dt} = C_{ng}^x = \frac{\partial\omega}{\partial k}$ and $\frac{dz}{dt} = C_{ng}^z = \frac{\partial\omega}{\partial m}$. The slope of ray paths in the (x,z) plane becomes:

$$\frac{dz}{dx} = \frac{2k}{m} = \frac{2kc_n}{N} \tag{A.4}$$

Therefore, the wave energy originating at the surface propagates downward towards the west with steeper slope for weaker stratification or lower latitude. Fig. A1 presents the theoretical trajectories for the annual period at various latitudes and for a mean stratification taken from the model (CR). With the definition of the phase propagation in the zonal and vertical directions, and because the dispersion relation is non-dispersive in the long zonal wavelength limit, phase lines are parallel to WKB ray paths. This wave propaga-

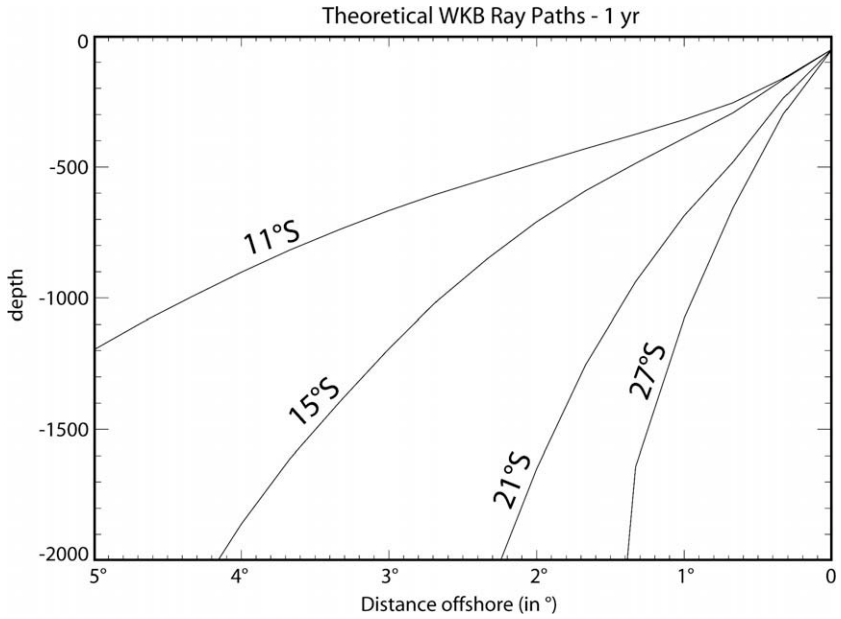

Fig. A1. Theoretical WKB trajectories for the annual period at 11°S, 15°S, 21°S and 27°S. The mean Brunt–vaïsälä frequency of the model and the mean between the first and second baroclinic mode phase speed were used to derive the local slope of the trajectories.

tion provides a mechanism by which low-frequency energy generated by surface wind is transmitted into the deep ocean.

References

Bentamy, A., Quilfen, Y., Gohin, F., Grima, N., Lenaour, M., Servain, J., 1996. Determination and validation of average wind fields from ERS-1 scatterometer measurements. Global Atmos. Ocean Syst. 4, 1–29.

Blanco, J.L., Thomas, A.C., Carr, M.-E., Strub, P.T., 2002. Hydrographic conditions off northern Chile during the 1996–1998 El Niño and La Niña events. J. Geophys. Res. 107 (C3), 89–90. doi:10.1029/2001.JC001002.

Carr, M.-E., 2002. Estimation of potential productivity in eastern boundary currents using remote sensing. Deep Sea Res. Pt. II 49, 59–80.

Cerovecki, I., de Szoeke, R., 2006. Initially forced long planetary waves in the presence of nonzonal mean flow. J. Phys. Oceanogr. 36, 507–525.

Chaigneau, A., Pizarro, O., 2005. Mean surface circulation and mesoscale turbulent flow characteristics in the eastern South Pacific from satellite tracked drifters. J. Geophys. Res. 110 (C5), C05014. doi:10.1029/2004JC002628.

Chelton, D.B., Schlax, M.G., 1996. Global observations of oceanic Rossby waves. Science 272, 234–238.

Chelton, D.B., deSzoeke, R.A., Schlax, M.G., Naggar, K.El., Siwertz, N., 1998. Geographical variability of the first-baroclinic Rossby radius of deformation. J. Phys. Oceanogr. 28, 433–460.

Clarke, A.J., Shi, C., 1991. Critical frequencies at ocean boundaries. J. Geophys. Res. 96, 10731–10738.

ColindeVerdiere, A., Tailleux, R., 2006. The interaction of a baroclinic mean flow with long Rossby waves. J. Phys. Oceanogr. 35, 865–879.

Conkright, M.E., Locarnini, R.A., Garcia, H.E., O'Brien, T.D., Boyer, T.P., Stephens, C., Antonov, J.I., 2002. World Ocean Atlas 2001: Objective Analyses, Data Statistics, and Figures. NOAA, Silver Spring, MD (CD-ROM).

de Boyer Montégut, C., Madec, G., Fischer, A.S., Lazar, A., Iudicone, 2004. Mixed layer depth over the global ocean: an examination of profile data and a profile-based climatology. J. Geophys. Res. 109, C12003. doi:10.1029/2004JC002378.

deSzoeke, R.A., Chelton, D., 1999. The modification of long planetary waves by homogeneous potential vorticity layers. J. Phys. Oceanogr. 29, 500–511.

Dewitte, B., 1998. Rôle de la structure verticale de l'océan sur la variabilité basse fréquence du Pacifique tropical. Ph.D. Thesis, University of Toulouse, 237 pp.

Dewitte, B., Reverdin, G., 2000. Vertically propagating annual and interannual variability in an OGCM simulation of the tropical Pacific in 1985–1994. J. Phys. Oceanogr. 30, 1562–1581.

Dewitte, B., Reverdin, G., Maes, C., 1999. Vertical structure of an OGCM simulation of the equatorial Pacific Ocean in 1985–1994. J. Phys. Oceanogr. 29, 1542–1570.

Eliassen, A., Palm, E., 1960. On the transfer of energy in stationary mountain waves. Geofys. Publ. 22 (3), 1–23.

Helly, J.J., Levin, L.A., 2004. Global distribution of naturally occurring marine hypoxia on continental margins. Deep Sea Res. Pt. I 51, 1159–1168.

Horel, J.D., 1984. Complex principal component analysis: theory and examples. J. Climate Appl. Meteorol. 23, 1660–1673.

Huyer, A., Smith, R.L., Paluszkiewicz, T., 1987. Coastal upwelling off Peru during normal and El Niño times 1981–1984. J. Geophys. Res. 92, 14297–14307.

Huyer, A., Knoll, M., Paluszkiewicz, T., Smith, R.L., 1991. The Peru Undercurrent: a study in variability. Deep Sea Res. 38 (Suppl. 1), 247–279.

Kalney et al., 1996. The NCEP/NCAR 40-year reanalysis project. Bull. Am. Meteorol. Soc. 74, 789–799.

Kessler, W.S., McCreary, J.P., 1993. The annual wind-driven Rossby wave in the subthermocline equatorial Pacific. J. Phys. Oceanogr. 23, 1192–1207.

Kessler, W.S., Rothstein, L.M., Chen, D., 1998. The annual cycle of SST in the eastern tropical Pacific, diagnosed in an ocean GCM. J. Climate 11, 777–799.

Killworth, P.D., Blundell, J.R., 1999. The effect of bottom topography on the speed of long extratropical planetary waves. J. Phys. Oceanogr. 29, 2689–2710.

Killworth, P.D., Chelton, D.B., deSzoeke, R.A., 1997. The speed of observed and theoretical long extra-tropical planetary waves. J. Phys. Oceanogr. 27, 1946–1966.

Le Traon, P.Y., Nadal, F., Ducet, N., 1998. An improved mapping method of multi-satellite altimeter data. J. Atmos. Ocean. Technol. 15, 522–534.

Lengaigne, M., Boulanger, J.-P., Menkes, C., Masson, S., Madec, G., Delecluse, P., 2002. Ocean response to the March 1997 Westerly Wind Event. J. Geophys. Res. 107 (C11). doi:10.1029/2001JC000841.

Levitus, S., Boyer, T.P., Conkright, M.E., O'Brien, T., Antonov, J., Stephens, C., Stathoplos, L., Johnson, D., Gelfeld, R., 1998. World Ocean Database 1998, vol. 1: Introduction. NOAA Atlas NESDIS 18. US Government Printing Office, Washington, DC.

Lighthill, M.J., 1969. Dynamical response of the Indian Ocean to the onset of the southwest monsoon. Philos. Trans. Roy. Soc. London, Ser. A 265, 45–92.

Madec, G., Delecluse, P., Imbard, M., Lévy, C., 1998. OPA 8.1 Ocean General Circulation Model reference manual. Note du Pôle de Modélisation, Institut Pierre-Simon Laplace, No. 11, 99 pp.

McCreary, J.P., 1981. A linear stratified ocean model of the Coastal Undercurrent. Philos. Trans. R. Soc. Lond. 302A, 385–413.

McCreary, J., 1984. Equatorial beams. J. Mar. Res. 42, 395–430.

Moore, D., Philander, S., 1977. Modelling the tropical ocean circulation. Sea 6, 319–361.

Penven, P., Pasapera, J., Tam, J., Echevin, V., 2005. Mean circulation, seasonal cycle and mesoscale dynamics of the Peruvian Upwelling System: a modelling approach. J. Geophys. Res. 110, C10021. doi:10.1029/2005JC002945.

Pizarro, O., Montecinos, A., 2004. Interdecadal variability of the thermocline along the west coast of South America. Geophys. Res. Lett. 31, L20307.

Pizarro, O., Clarke, A.J., Gorder, S.V., 2001. El Niño sea level and currents along the South American coast: comparison of observations with theory. J. Phys. Oceanogr. 31, 1891–1903.

Pizarro, O., Shaffer, G., Dewitte, B., Ramos, M., 2002. Dynamics of seasonal and interannual variability of the Peru–Chile Undercurrent. Geophys. Res. Lett. 29 (12). doi:10.1029/2002GL014790.

Qiu, B., Miao, W., Muller, P., 1997. Propagation and decay of forced and free baroclinic Rossby waves in off-equatorial oceans. J. Phys. Oceanogr. 27, 2405–2417.

Ramos, M., Pizarro, O., Bravo, L., Dewitte, B., 2006. Seasonal variability of the permanent thermocline off northern Chile. Geophys. Res. Lett. 33, L09608. doi:10.1029/2006GL025882.

Reynolds, R.W., Smith, T.M., 1994. Improved global sea surface temperature analyses. J. Climate 7, 929–948.

Roden, G.I., 1962. Oceanographic aspects of the eastern equatorial Pacific. Geophys. Int. 2, 77–92.
Shaffer, G.O., Pizarro, L., Djurfeldt, S., Salinas, Rutlland J., 1997. Circulation and low-frequency variability near the Chilean coast: remotely forced fluctuations during the 1991–1992 El Niño. J. Phys. Oceanogr. 27, 217–235.
Shaffer, G.S., Hormazabal, O., Pizarro, Salinas, S., 1999. Seasonal and interannual variability of currents and temperature off central Chile. J. Geophys. Res. 104 (C12), 29951–29961.
Silva, N., Neshyba, S., 1979. On the southernmost extension of the Perú–Chile Undercurrent. Deep Sea Res. 26, 1387–1393.
Stammer, D., 1997. Global characteristics of ocean variability estimated from regional TOPEX/POSEIDON altimeter measurements. J. Phys. Oceanogr. 27 (8), 1743–1769.
Strub, P.T., Mesias, J.M., Montecino, V., Rutllant, J., Salinas, S., 1998. Coastal ocean circulation off western South America. In: Robinson, A.R., Brink, K.H. (Eds.), The Sea, vol. 11. John Wiley, New York, pp. 273–313.
Tailleux, R., McWilliams, J.C., 2001. The effect of bottom pressure decoupling on the speed of extratropical, baroclinic Rossby waves. J. Phys. Oceanogr. 31, 1461–1476.
Takahashi, K., 2005. The annual cycle of heat content in the Peru Current region. J. Climate 18 (23), 4937–4954.
Thompson, L.K., Kelly, A., Darr, D., Hallberg, R., 2002. Buoyancy and mixed layer effects on the Sea Surface Height Response in an isopycnal model of the North Pacific. J. Phys. Oceanogr. 32, 3657–3670.
Vazquez, J., Tran, A., Sumagaysay, R., Smith, E.A., Hamilton, M., 1995. NOAA/NASA AVHRR oceans pathfinder sea surface temperature data set user's guide version 12. JPL Technical Report, p. 55.
Vega, A., duPenhoat, Y., Dewitte, B., Pizarro, O., 2003. Equatorial forcing of interannual Rossby waves in the South eastern Pacific. Geophys. Res. Lett. 30 (5), 1197–1200.
Weare, B.C., Nasstrom, J.S., 1982. Examples of extended empirical orthogonal function analysis. Mon. Weath. Rev. 110, 481–485.
Wunsch, C., 1997. The vertical partition of oceanic horizontal kinetic energy. J. Phys. Oceanogr. 27, 1770–1794.
Wyrtki, K., 1963. The horizontal and vertical field of motion in the Peru Current. Bull. Scripps Inst. Oceanogr. Univ. Calif. 8 (4), 313–346.
Xie, P., Arkin, P.A., 1996. Analysis of global monthly precipitation using gauge observations, satellite estimates, and numerical model predictions. J. Climate 9, 840–858.
Yeager, S.G., Large, W.G., 2004. Late-winter generation of spiciness on subducted isopycnals. J. Phys. Oceanogr. 34, 1528–1547.